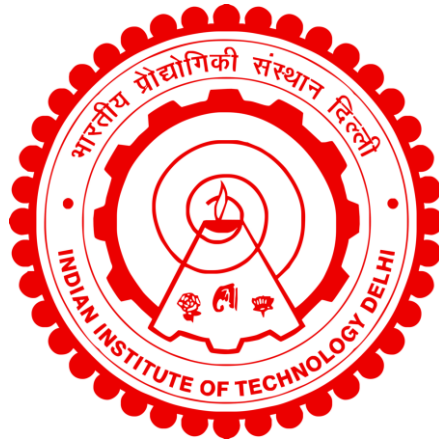


**SPUTTERED GROWTH OF TOPOLOGICAL INSULATORS
(Sb₂Te₃ & Bi₂Te₃), LIGHT METAL Zr and 2D VAN DER
WAALS FERROMAGNET CrTe₂ BASED
HETEROSTRUCTURES FOR SPIN TRANSPORT STUDIES**

NAKUL KUMAR



**DEPARTMENT OF PHYSICS
INDIAN INSTITUTE OF TECHNOLOGY DELHI
APRIL 2026**

© Indian Institute of Technology Delhi (IITD), New Delhi, 2026

**Sputtered Growth of Topological Insulators (Sb_2Te_3
& Bi_2Te_3), Light Metal Zr and 2D van der Waal
Ferromagnet CrTe_2 based Heterostructures for Spin
Transport Studies**

by

NAKUL KUMAR

Department of Physics

submitted

In the fulfilment of the requirement of the degree of
the Doctor of Philosophy to the



INDIAN INSTITUTE OF TECHNOLOGY DELHI

APRIL 2026

Dedicated to my Family

Certificate

This is to certify that the thesis entitled “**Sputtered Growth of Topological Insulators (Sb_2Te_3 & Bi_2Te_3), Light Metal Zr and 2D van der Waal Ferromagnet CrTe_2 based Heterostructures for Spin Transport Studies**”, submitted by **Mr. Nakul Kumar (2020PHZ8348)** to the **Indian Institute of Technology Delhi, New Delhi India**, in partial fulfillment of the requirements for the award of the degree of **Doctor of Philosophy in Physics**, embodies the results of original and bona fide research carried out by him under my supervision and guidance. He has satisfactorily fulfilled all the prescribed requirements for the submission of this thesis, which, in my considered opinion, meets the standards expected for the award of the doctoral degree.

Furthermore, I certify that the work presented in this thesis, in whole or in part, has not been submitted to any other University or Institute for the award of any degree or diploma.

Prof. Sujeet Chaudhary
Professor
Department of Physics
Indian Institute of Technology Delhi
New Delhi - 110016
India

Date:

Acknowledgements

Writing this acknowledgment fills me with deep emotion, as it takes me back through the memories of the past five years. My Ph.D. journey and my life at IIT Delhi have been truly remarkable, and it is entirely because of the wonderful people who have been part of it. It is difficult to capture my gratitude in just a few lines, but I hope these words reflect at least a part of what I feel.

I would first like to express my deepest gratitude to my mentor, **Prof. Sujeet Chaudhary**, for giving me the opportunity to pursue my Ph.D. research in the Thin Film Laboratory (TFL). I am sincerely thankful to him for the academic freedom he provided for trusting me with new ideas, encouraging me to take risks, and allowing me to learn through mistakes.

In the initial years of my Ph.D., Sujeet Sir guided me with difficult but meaningful tasks and helped me develop the discipline needed to complete them on time. His questions always pushed me to think deeply and critically. The rigorous training I received from him shaped my scientific approach, strengthened my experimental skills, and helped me grow into a more confident and independent researcher. His constant encouragement, constructive criticism, and commitment to quality have played a major role in my academic and personality developments.

I am grateful to the **Department of Physics, IIT Delhi**, for the privilege of working in such an enriching academic environment. I sincerely thank **Council of Scientific & Industrial Research (CSIR)** for supporting my research through the fellowship. I am also thankful to IIT Delhi for funding my participation in national and international conferences, which helped broaden my academic exposure. The support and facilities provided by **NRF** and **CRF** were essential for conducting the experimental part of this work.

My heartfelt thanks go to the members of my SRC committee members Prof. Santanu Ghosh, Prof. Kaustuv Manna, and Prof. Nirat Ray for their valuable suggestions, feedback, and discussions at every stage of my research. Their guidance helped refine the direction and quality of my work.

I also thank Prof. Sujit Manna for the opportunity to independently operate the departmental PPMS facility. My sincere thanks to Dr. Dinesh Dixit (PPMS Lab) and Dr. Veer Singh (SIMS) at the Sonipat CRF Facility for their consistent technical support and collaboration. I would like to thank Dr. Anup Choudhary (IUAC) who helped me in cryogenics instrumentations.

I am truly grateful to **Mr. Nagendra Chaudhary** for his technical help and warm interactions. His advice both scientific and personal made my Ph.D. life much smoother.

A very special note of thanks goes to **Dr. Lalit Pandey** and my lab mate **Dr. Nikita Sharma**, who made this entire journey meaningful and memorable. Nikita's excellent experimental and LabVIEW skills were crucial for many parts of my work, and my long discussions with Dr. Lalit Pandey helped sharpen my scientific understanding. My sincere thanks also go to Dr. Soumyarup Hait for teaching me how to approach tasks calmly, and to Dr. Nanhe Kumar Gupta for inspiring me through his disciplined and dedicated work style. I am equally thankful to Dr. Viresh Mishra and Amar Kumar, who were not just colleagues but wonderful friends through countless hours in the lab.

I gratefully acknowledge Dr. Sajid Hussain, Dr. Vineet Barwal, Dr. Ekta, Dr. Pradeep Sharma, and Dr. Sanjay Kedia for creating a friendly and academically stimulating environment. I extend warm thanks to Harjinder, Amir, and Badshah, whose project work became a shared learning experience and enriched the collaborative atmosphere in the lab.

To my juniors **Subhashish, Abhay, Mitali, Saurav, Vidhi, Shweta, Prashant Joshi, Bhaskar, Priya and, importantly, our post doc senior Dr. Nidhi Shukla**, I am thankful for the fresh energy and enthusiasm they brought, especially in the final stage of my Ph.D. Their curiosity and dedication often motivated me to keep moving forward.

I owe a deep sense of gratitude to my close friends **Ravi Meena, Avantika, Sarita, Manish, Vijay, Sakshi, Kaushalya, and Ekta**, who stood by me like family. Their emotional support, scientific discussions, and constant encouragement kept me going during challenging times.

Finally, I am forever grateful to **my parents, my brother, my sisters, and my schoolteachers**, especially my Physics teacher **Sanjeev Guru ji** and english teacher **Rahul Tyagi Ji**, who have been my strongest pillars of support. Their unconditional love, patience, and belief in me have been the foundation of everything I have achieved.

Nakul Kuma

(April 2026)

Abstract

Topological quantum materials, enriched by strong spin-orbit interactions and emergent Berry-curvature driven phenomena, promise a transformative pathway toward ultrafast, low-power spin-based information technologies. In this thesis, a comprehensive exploration of spin, orbital, and topological transport in engineered thin-film heterostructures is undertaken to elucidate the mechanisms governing spin-to-charge conversion, orbital current generation, and Berry-curvature induced transport anomalies in two dimensions (2D) van der Waals (vdW) Ferromagnetic (FM) materials.

The thesis first examines interface-engineered $\text{Al}_2\text{O}_3(0001)/\text{Sb}_2\text{Te}_3(20\text{nm})/\text{Ru}(0-12\text{nm})/\text{Co}_{20}\text{Fe}_{20}\text{B}_{20}(20\text{nm})/\text{Ru}(4\text{nm})$, TI/FM heterostructures grown via DC magnetron co-sputtering, where a remarkably high spin-to-charge conversion (SCC) efficiency is demonstrated at room temperature. A pronounced enhancement in the charge current density emerges specifically at a 4-nm Ru interlayer thickness, beyond which the SCC efficiency decreases with additional Ru thickness. Quantitative analyses using inverse spin Hall effect (ISHE) reveal nearly 5 times enhancement in SCC upon the insertion of a 4-nm Ru layer, yielding an inverse Edelstein length (λ_{IEE}) of 0.19 ± 0.01 nm comparable to or exceeding reported values in prominent TI/FM systems. Longitudinal spin Seebeck effect (LSSE) measurements corroborate these trends and further disentangle the pure TI-driven Seebeck contribution from the anomalous Nernst effect originating in the ferromagnetic $\text{Co}_{20}\text{Fe}_{20}\text{B}_{20}$ (CFB).

Building upon these insights, the thesis next delves into the simultaneous generation and interconversion of spin and orbital currents in $\text{Zr}(t=2-20\text{nm})/\text{CFB}$, $\text{Zr}(t)/\text{Pt}/\text{CFB}$, and $\text{Zr}(t)/\text{Pt}/\text{CFB}/\text{Pt}$ stacks, examined via spin-orbital pumping ferromagnetic resonance (SOP-FMR) and longitudinal spin-orbital Seebeck (LSOSE) measurements. The moderate spin-orbit coupling in CFB enables the concurrent injection of spin and orbital currents into adjacent layers, where their transformation into charge currents is governed by the interplay of ISHE, inverse orbital Hall effect (IOHE), and inverse orbital Rashba-Edelstein effect (IOREE). A striking increase in the orbital-dominated charge conversion appears when a Pt interlayer is introduced at the Zr/CFB interface, resulting in an enhancement of the effective Rashba-Edelstein length $\lambda_{IORE}^{\text{Zr-eff}}$ from ~ 0.29 nm in $\text{Zr}(4.5)/\text{CFB}(20)$ to ~ 1.98 nm and ~ 1.70 nm in $\text{Zr}(4.5)/\text{Pt}(2)/\text{CFB}(20)$ and $\text{Zr}(4.5)/\text{Pt}(2)/\text{CFB}(20)/\text{Pt}(2)$, respectively representing an almost 500% increase. These results, consistently validated through spin-orbital Seebeck

measurements, uncover new avenues wherein orbital angular momentum rather than spin alone can be harnessed for highly efficient charge-current generation, offering an extended design space for orbital-spin hybrid devices.

The thesis then shifts focus to the intriguing physics of layered vdW ferromagnets, with CrTe₂ (CT) thin films synthesized for the first time via DC magnetron sputtering. CT films of thickness 20-60 nm grown on Si(100) at 350°C and 400°C yield low-crystallinity (LC) and high-crystallinity (HC) samples, respectively. The crystalline quality profoundly influences the magnetic and electronic behavior, with Curie temperatures T_C of ~140 K (LC) and ~220 K (HC), and robust perpendicular magnetic anisotropy persisting across both series. Notably, the HC-CT films exhibit a dramatic sign reversal in anomalous Hall effect (AHE) below 100 K, attributed to a temperature-driven modification of Berry curvature in momentum space. Electron-magnon scattering dominates their low-temperature resistivity, contrasting with the semiconducting behavior of LC-CT films. Furthermore, the emergent topological Hall signatures in CrTe₂/Bi₂Te₃ heterostructures, where the interfacial coupling between the 2D ferromagnet and the topological insulator generates a nontrivial real-space Berry curvature environment conducive to chiral spin textures. The synergy between the strong spin-orbit coupling of Bi₂Te₃ and the intrinsic magnetic order of polycrystalline and highly crystalline CrTe₂ stabilizes nanoscale noncollinear spin configurations, leading to a distinct topological Hall contribution superimposed upon the anomalous and ordinary Hall responses. These findings position CrTe₂/Bi₂Te₃ interfaces as promising candidates for topological spintronic memory elements and skyrmion-based logic platforms. These sputtered HC-CT films not only recapitulate but in certain aspects rival the magnetic and topological attributes of MBE- and CVD-grown films, establishing sputtering as an industrially scalable pathway for vdW ferromagnet integration.

Collectively, the investigations presented herein construct a unified and experimentally substantiated picture of how spin, orbital, and topological degrees of freedom intertwine in thin film heterostructures. Through a combination of interface engineering, material-quality optimization, and comprehensive spectroscopic and transport measurements, this work establishes foundational principles and practical pathways for designing next-generation spintronic, orbitronic, and topological devices capable of meeting the stringent demands of quantum-information processing and energy-efficient computing.

सार

प्रबल स्पिन-कक्षा अंतःक्रियाओं (spin-orbit interactions) तथा उद्भूत Berry-curvature प्रेरित घटनाओं से समृद्ध टोपोलॉजिकल क्वांटम पदार्थ, अति-तीव्र (ultrafast), निम्न-ऊर्जा (low-power) स्पिन-आधारित सूचना-प्रौद्योगिकियों की दिशा में एक रूपांतरणकारी मार्ग प्रस्तुत करते हैं। इस शोधप्रबंध में अभिकल्पित पतली-परत हेटरोस्ट्रक्चरों में स्पिन, कक्षीय (orbital), तथा टोपोलॉजिकल परिवहन का व्यापक अध्ययन किया गया है, ताकि स्पिन-से-आवेश रूपांतरण, कक्षीय धारा उत्पत्ति, तथा द्वि-आयामी (2D) वान डर वाल्स (vdW) फेरोमैग्नेटिक (FM) पदार्थों में Berry-curvature प्रेरित परिवहन विसंगतियों को नियंत्रित करने वाले तंत्रों को समझा जा सके।

शोधप्रबंध का प्रथम भाग इंटरफ़ेस-अभिकल्पित $\text{Al}_2\text{O}_3(0001)/\text{Sb}_2\text{Te}_3(20\text{nm})/\text{Ru}(0-12\text{nm})/\text{Co}_{20}\text{Fe}_{20}\text{B}_{20}(20\text{nm})/\text{Ru}(4\text{nm})$ टोपोलॉजिकल इंसुलेटर/फेरोमैग्नेट (TI/FM) हेटरोस्ट्रक्चरों की जांच करता है, जिन्हें DC magnetron co-sputtering द्वारा विकसित किया गया। इन संरचनाओं में कक्ष-ताप (room temperature) पर अत्यंत उच्च spin-to-charge conversion (SCC) दक्षता प्रदर्शित की गई है। विशेष रूप से 4-nm Ru अंतर-परत मोटाई पर आवेश धारा घनत्व में उल्लेखनीय वृद्धि देखी गई, जिसके बाद Ru की मोटाई बढ़ाने पर SCC दक्षता घटती चली जाती है। Inverse spin Hall effect (ISHE) पर आधारित मात्रात्मक विश्लेषण से स्पष्ट हुआ कि 4-nm Ru परत के समावेशन से SCC में लगभग 5 गुना वृद्धि होती है, जिसके परिणामस्वरूप inverse Edelstein length (λ_{IEE}) 0.19 ± 0.01 nm प्राप्त होती है, जो प्रमुख TI/FM प्रणालियों में रिपोर्ट किए गए मानों के तुल्य अथवा उनसे अधिक है। Longitudinal spin Seebeck effect (LSSE) माप इन प्रवृत्तियों की पुष्टि करते हैं और साथ ही शुद्ध TI-प्रेरित Seebeck योगदान को फेरोमैग्नेटिक $\text{Co}_{20}\text{Fe}_{20}\text{B}_{20}$ (CFB) में उत्पन्न anomalous Nernst effect से पृथक भी करते हैं।

इन निष्कर्षों के आधार पर, शोधप्रबंध का अगला भाग $\text{Zr}(t=2-20\text{nm})/\text{CFB}$, $\text{Zr}(t)/\text{Pt}/\text{CFB}$, तथा $\text{Zr}(t)/\text{Pt}/\text{CFB}/\text{Pt}$ संरचनाओं में स्पिन तथा कक्षीय धाराओं की समकालिक उत्पत्ति और परस्पर रूपांतरण का अध्ययन करता है। इन प्रणालियों की जांच spin-orbital pumping ferromagnetic resonance (SOP-FMR) तथा longitudinal spin-orbital Seebeck (LSOSE) मापों द्वारा की गई। CFB में मध्यम spin-orbit coupling होने के कारण स्पिन और कक्षीय दोनों धाराएँ समीपवर्ती परतों में एक साथ प्रविष्ट हो सकती हैं, जहाँ उनका आवेश धारा में रूपांतरण ISHE, inverse orbital Hall effect (IOHE), तथा inverse orbital Rashba-Edelstein effect (IOREE) की परस्पर क्रिया द्वारा नियंत्रित होता है। विशेष रूप से, जब Zr/CFB इंटरफ़ेस पर Pt अंतर-परत जोड़ी गई, तब orbital-dominated charge conversion में उल्लेखनीय वृद्धि देखी गई। इसके फलस्वरूप प्रभावी Rashba-Edelstein length $\lambda_{IORE}^{\text{Zr-eff}}$ लगभग 0.29 nm [$\text{Zr}(4.5)/\text{CFB}(20)$] से बढ़कर लगभग 1.98 nm तथा लगभग 1.70 nm [क्रमशः $\text{Zr}(4.5)/\text{Pt}(2)/\text{CFB}(20)$ और $\text{Zr}(4.5)/\text{Pt}(2)/\text{CFB}(20)/\text{Pt}(2)$] हो गई, जो लगभग 500% वृद्धि का द्योतक है। ये परिणाम, जिन्हें spin-orbital Seebeck मापों द्वारा भी सुसंगत रूप से सत्यापित किया गया, इस तथ्य को उद्घाटित करते हैं कि केवल स्पिन ही नहीं, बल्कि कक्षीय कोणीय संवेग (orbital angular momentum) को भी अत्यधिक दक्ष आवेश-धारा जनन हेतु उपयोग में लाया जा सकता है। इस प्रकार यह कार्य orbital-spin hybrid युक्तियों के लिए एक विस्तृत अभिकल्पना-क्षेत्र प्रस्तुत करता है।

इसके पश्चात शोधप्रबंध का ध्यान स्तरित vdW फेरोमैग्नेटों के रोचक भौतिकी-विज्ञान की ओर केंद्रित होता है, जहाँ CrTe₂ (CT) पतली परतों का प्रथम बार DC magnetron sputtering द्वारा संश्लेषण किया गया। Si(100) पर 350°C और 400°C पर विकसित 20-60 nm मोटाई वाली CT परतों ने क्रमशः निम्न-स्फटिकीयता (low-crystallinity, LC) तथा उच्च-स्फटिकीयता (high-crystallinity, HC) नमूने उत्पन्न किए। स्फटिकीय गुणवत्ता ने इनके चुम्बकीय और वैद्युतिक व्यवहार पर गहरा प्रभाव डाला; LC तथा HC नमूनों के लिए Curie तापक्रम (TC) क्रमशः लगभग 140 K और लगभग 220 K प्राप्त हुआ, और दोनों श्रेणियों में प्रबल perpendicular magnetic anisotropy विद्यमान रही। विशेष रूप से HC-CT परतों में 100 K से नीचे anomalous Hall effect (AHE) के चिह्न में नाटकीय उलटाव देखा गया, जिसे momentum space में Berry curvature के ताप-प्रेरित परिवर्तन से संबद्ध किया गया है। निम्न ताप पर इनके प्रतिरोध में electron-magnon scattering प्रमुख भूमिका निभाती है, जो LC-CT परतों के अर्धचालकीय व्यवहार से स्पष्टतः भिन्न है।

इसके अतिरिक्त, CrTe₂/Bi₂Te₃ हेटरोस्ट्रक्चरों में उद्भूत topological Hall signatures भी देखे गए, जहाँ 2D फेरोमैग्नेट और टोपोलॉजिकल इंसुलेटर के मध्य अंतःपृष्ठीय युग्मन एक ऐसी nontrivial real-space Berry curvature अवस्था निर्मित करता है जो chiral spin textures के लिए अनुकूल है। Bi₂Te₃ की प्रबल spin-orbit coupling तथा polycrystalline और highly crystalline CrTe₂ की अंतर्निहित चुम्बकीय व्यवस्था के परस्पर समन्वय से नैनो-स्तरीय noncollinear spin configurations स्थिर होती हैं, जिसके परिणामस्वरूप anomalous तथा ordinary Hall response के ऊपर आरोपित एक स्पष्ट topological Hall contribution प्राप्त होती है। ये निष्कर्ष CrTe₂/Bi₂Te₃ अंतःपृष्ठों को topological spintronic memory तत्वों तथा skyrmion-आधारित logic platforms के लिए अत्यंत आशाजनक प्रत्याशी के रूप में स्थापित करते हैं। ये sputtered HC-CT परतें न केवल MBE और CVD द्वारा विकसित परतों के चुम्बकीय और टोपोलॉजिकल गुणों की पुनरावृत्ति करती हैं, बल्कि कुछ पक्षों में उनसे प्रतिस्पर्धा भी करती हैं। इस प्रकार sputtering, vdW फेरोमैग्नेट एकीकरण के लिए एक औद्योगिक रूप से स्केलेबल मार्ग के रूप में स्थापित होती है।

समग्र रूप से, इस शोधप्रबंध में प्रस्तुत अध्ययन यह स्पष्ट और प्रायोगिक रूप से प्रमाणित चित्र निर्मित करते हैं कि किस प्रकार स्पिन, कक्षीय और टोपोलॉजिकल स्वतंत्रताएँ पतली-परत हेटरोस्ट्रक्चरों में परस्पर गुंथी हुई हैं। इंटरफ़ेस अभिकल्पना, पदार्थ-गुणवत्ता अनुकूलन, तथा व्यापक स्पेक्ट्रोस्कोपिक और परिवहन मापों के संयोजन द्वारा यह कार्य अगली पीढ़ी की spintronic, orbitronic, और topological युक्तियों के अभिकल्पन हेतु मूलभूत सिद्धांतों और व्यावहारिक मार्गों की स्थापना करता है, जो quantum-information processing तथा ऊर्जा-दक्ष कंप्यूटिंग की कठोर आवश्यकताओं को पूरा करने में सक्षम हो सकती हैं।

Table of Contents

Certificate	i
Acknowledgements	ii
Abstract	iv
List of Figures	xiii
List of Tables	xxvii
Chapter 1 Introduction	1
1.1 Fundamental of Spintronics	2
1.2 Spin Current	3
1.3 Generation of Spin Current	5
1.3.1 Magnetization Dynamics via Ferromagnetic Resonance	5
1.3.2 Spin Pumping	7
1.4 Spin Hall Effect	8
1.4.1 Intrinsic Mechanism (Berry phase)	10
1.4.2 Skew Scattering	10
1.4.3 Side Jump	11
1.4.4 Interfacial Rashba Edelstien Effect	11
1.5 Detection of Spin Current	12
1.5.1 Inverse Spin Hall Effect	13
1.5.2 Spin Seebeck Effect	14
1.5.3 Longitudinal Spin Seebeck Effect	15
1.6 Orbital Hall Effect and its Detection	16
1.7 Application of Spin Current Devices	17
1.7.1 Spin Transfer Torque	18
1.7.2 Spin Orbit Torque	19

1.8	Choice of Materials	21
1.8.1	Topological Insulator	21
1.8.1.1	Topological Insulators and Their Surface State Properties	22
1.8.1.2	Topological as Spin to Charge Conversion Facilitator	23
1.8.1.3	Role of Time Reversal Breaking in Topological Insulators via Magnetic Proximity Effect	24
1.8.2	Heavy Metals	25
1.8.3	Light Transition Metals as Orbital to Charge	26
1.8.4	Two-Dimensional van der Waals Materials	27
1.8.4.1	van der Waals CrxTey	28
1.8.4.2	Magnetism in van der Waals Materials	31
1.8.5	Magnetic Anisotropy in 2D van der Waals materials	32
1.8.5.1	Magneto-crystalline Anisotropy	33
1.8.5.2	Dzyaloshinskii-Moriya Interaction	34
1.9	Literature Survey and Motivation	36
1.10	Objective of Thesis	40
1.10.1	Organization of Thesis	40
	References	44
	Chapter 2 Experimental Details	54
2.1	Thin Film Deposition Technique	55
2.1.1	Sputtering	55
2.2	Material Characterization Techniques	58
2.2.1	X-ray Diffraction	58
2.2.2	X-Ray Reflectivity	61
2.2.3	Electron Probe Microanalyzer (EPMA)	63
2.2.4	Time of Flight-Secondary Ion Mass Spectrometry (TOF-SIMS)	64

2.3	Measurement Techniques	65
2.3.1	Ferromagnetic Resonance (FMR) Measurement	65
2.3.2	Inverse Spin Hall Effect Measurement	68
2.3.2.1	Setup Details	68
2.3.3	Spin Seebeck Effect (SSE) Measurements	69
2.3.4	Transport Measurements	71
2.3.4.1	Resistivity Measurement	71
2.3.4.2	Anomalous Hall Effect	72
2.3.4.3	Magneto-resistance Measurements	73
2.3.5	Magnetic Measurements	74
	References	77

Chapter 3 Tuning of spin-to-charge conversion in topological insulator based $\text{Sb}_2\text{Te}_3/\text{Ru}(t)/\text{Co}_{60}\text{Fe}_{20}\text{B}_{20}/\text{Ru}$ heterostructures investigated by inverse spin Hall effect and spin Seebeck effect 79

3.1	Introduction	80
3.2	Growth Methodology	82
3.3	Results and Discussion	84
3.3.1	Structural Analysis	84
3.3.2	Topological Properties analysis of Sb_2Te_3 film through magneto-transport measurements	86
3.3.3	Ferromagnetic resonance study	88
3.3.4	Spin to charge conversion: SP-FMR through ISHE	91
3.3.5	Effect of Ru interlayer on spin-to-charge conversion efficiency	94
3.3.6	Spin Seebeck Measurements	100
3.4	Conclusion	106
	Reference	107

Chapter 4	Orbital to charge conversion in the light metal Zr using spin pumping ferromagnetic resonance and spin Seebeck measurements	114
4.1	Introduction	115
4.2	Experimental section	117
4.2.1	Sample Growth and Characterization	117
4.3	Results and Discussion	119
4.3.1	Spin-orbital pumping ferromagnetic resonance measurements	119
4.3.2	Longitudinal Spin and Orbital Seebeck Effect (LSOSE) measurements	131
4.4	Summary	135
	References	137
Chapter 5	Growth and investigation of 2D van der Waal CrTe₂ ferromagnet via DC sputtering and their study of crystallinity dependent magnetic and-transport properties	142
5.1	Introduction	143
5.2	Growth and structural characterization	145
5.3	Results and Discussion	148
5.3.1	Magnetic Properties	148
5.3.1.1	Magnetic Properties of the LC-CT series Films	148
5.3.1.2	Magnetic Properties of HC-CT series Films	150
5.3.2	Transport Properties	152
5.3.2.1	Temperature Dependent Resistivity, Discussion and Analysis	156
5.4	Conclusion	159
	References	160
Chapter 6	Topological Hall signature in crystallinity dependent van der Waal CrTe₂/Bi₂Te₃ heterostructures	165
6.1	Introduction	166
6.2	Experimental Details	168

6.3	Results and Discussion	170
6.4	Conclusion	177
	References	178
Chapter 7 Summary and Future Perspective		180
7.1	Summary	181
7.2	Future Perspective	184
Appendix A Supplementary details		185
A1	Heterostructure Characterization and Ferromagnetic Resonance	185
A2	Spin Orbital Pumping Voltage Measurements	189
A3	Longitudinal Spin Orbital Seebeck Effect	194
	References	195
Appendix B Other R & D Activities		197
B1	Resurrection of a completely damaged Quantum Design PPMS due to severe Water-flooding	197
B2	Home Built filament and Fluorescent screen for 50 keV RHEED system	205
Thesis Publications		209
Published/Under review/Submitted		209
Other Publications (not included in the thesis)		209
Peer Reviewed Conference Contributions		211
Author's Biography		212

List of Figures

Figure No.	Figure Caption	Page No.
1.1	Schematic representing the flow of (a) pure charge current (b) spin current (c) pure spin current densities in metals.	4
1.2	Schematic of magnetization dynamics (a) Applied magnetic field (H_{eff}), (b) Under the influence of microwave field h_{rf} along with H_{eff} at the resonance condition	6
1.3	Schematic of the FM/NM bilayer structure showing the spin pumping induced flow of spin current through the FM/NM interface.	7
1.4	Schematic showing the phenomenon of spin Hall effect i.e., generation of spin current density (J_s) originated from charge current density (J_c).	8
1.5	Types of spin dependent scattering: (a) Intrinsic mechanism because of Berry phase. Extrinsic mechanisms consist of (b) Skew jump and (c) Side jump scattering.	10
1.6	(a) Schematic illustration of Rashba spin-orbit coupling and the resulting spin-split electronic band structure. The structural inversion asymmetry lifts the spin degeneracy, producing two concentric Fermi contours with opposite spin-helicities. (b) The upper and lower Rashba-split bands exhibit chiral spin textures (clockwise and counterclockwise spin orientations). (c) When an external charge current J_c is applied, the nonequilibrium shift (Δk) in the Fermi surface induces a net spin accumulation (spin polarization) transverse to the driving current, giving rise to spin-orbit torque phenomena.	12
1.7	Schematic of the spin current injection from the FM layer to NM layer generated by spin pumping in the FM layer. This spin current is converted into the charge current in the NM layer via ISHE effect.	13
1.8	Schematic illustration of the LSSE effect: the LSSE produces a flow of spin angular momentum without a net charge flow. This pure spin current can then be converted into a measurable electrical voltage using the ISHE in an adjacent non-magnetic metal with strong spin-orbit coupling. Here,	15

- E_{ISHE} denote the electric fields generated by the ISHE effect, here, ∇T : temperature gradient, H : magnetic field, M : magnetization vector, and J_s : thermally generated spin current. (b) Represents the transverse spin Seeback effect phenomenon.
- 1.9** (a) Schematic illustration of the orbital Hall effect (OHE) in light metals. **16**
 (b) Schematic representation of the IOHE in light-metal heterostructures with ferromagnetic layers.(c) Schematic depiction of orbital-current generation arising from the interplay between the strong SOC in HM and its transfer into the LM, where the orbital current is subsequently converted into a charge current. In the LM, orbital currents are transformed into charge currents, while in the HM, spin currents are converted into charge currents via ISHE.
- 1.10** Schematic of the spin-transfer torque mechanism. An unpolarized current becomes spin-polarized after passing through the reference layer (FM1), and upon entering the free layer (FM2), the spin-flip process transfers angular momentum, switching the magnetization of the free layer. **18**
- 1.11** Comparison between SOT and STT-SOT device structures (a) SOT device, an in-plane charge current J_c flows through the heavy-metal/non-magnetic (NM) layer, generating a transverse spin current $J_s(z)$ via spin-orbit coupling, which exerts spin-orbit torque on the adjacent ferromagnetic (FM) layer to manipulate its magnetization. (b) In the STTSOT device, spin-orbit torque generated by the heavy-metal layer assists spin-transfer torque ISTT through the magnetic tunnel junction (MgO barrier) between the fixed and free ferromagnetic layers, enabling efficient switching and separate write/read paths. **20**
- 1.12** Classification of materials based on their electronic band structure. From left to right: (i) Insulator, characterized by a large band gap with the Fermi level located within the forbidden gap, semiconductor, in which a moderate band gap allows thermally activated excitation of electrons across the gap, semimetals, where doping introduces donor or acceptor states within the band gap enabling enhanced carrier concentration, metal, possessing partially filled bands or overlapping conduction and valence bands, resulting in high electrical conductivity; and topological material, **23**

	where the band inversion and symmetry-protected Dirac (or Weyl) points lead to gapless surface or edge states with spin-momentum locking.	
1.13	(a-c) Layered crystal structures viewed from the same direction, illustrating the periodic stacking separated by van der Waals gaps of CrTe ₂ , Sb ₂ Te ₃ and CrGeTe ₃ , respectively. The zig-zag atomic arrangement within each layer and the uniform interlayer spacing are visible.	28
1.14	van der Waals ferromagnetic ordering in 2D magnetic materials. (a) Ferromagnetic ordering (b) Antiferromagnetic ordering	29
1.15	(a) Schematic illustration of the DMI at a heavy-HM/FM interface, showing neighboring spins <i>S</i> ₁ and <i>S</i> ₂ experiencing an antisymmetric exchange interaction due to broken inversion symmetry and strong spin-orbit coupling. (b) Schematic magnetic texture demonstrating the formation of skyrmions in an HM/FM multilayer system, where interfacial DMI stabilizes chiral spin configurations with vortex-like topology.	34
2.1	Schematic of the Excel Instruments make DC magnetron sputtering system for deposition of thin films. The system is employed with 4 guns and other components related to the system are labelled in the figures.	56
2.2	(a) Real image of magnetron with the magnetic arrangement (at the periphery N pole of magnet and at the center a slug is there) (b) Simulated magnetic field profile of the magnetron seen from the side cross-sectional view	57
2.3	(a) Schematic of the incidence and diffraction of x-rays on parallel atomic planes with Miller indices (<i>hkl</i>) acting as coherent scatterers, resulting in diffraction under Bragg's condition. (b) Schematic representation of the X-ray diffractometer illustrating the key optical components on both the source and detector sides used during measurement.	59
2.4	(a) schematic of θ - 2θ (gonio mode) scan (b) Schematic of glancing angle GIXRD scan	60
2.5	(a) Schematic illustrating the refraction geometry, including incident and refracted beam directions, relevant angles, and wave-vector components for X-rays impinging from air onto a surface with refractive index $n < 1$. (b) Representative X-ray reflectivity (XRR) profile of a Sb ₂ Te ₃ thin film on Si(100), highlighting the key structural information extractable from XRR measurements.	61

2.6	Schematic of electron probe microanalyzer	63
2.7	Schematic of the SIMS measurement setup with illustration of each component	64
2.8	Schematic of the homebuilt in-plane FMR setup with all the equipment used measurement.	67
2.9	Schematic of the homebuilt inverse spin Hall effect measurement setup.	68
2.10	Schematic of the homebuilt Spin Seebeck effect measurement setup.	70
2.11	Four probe resistivity measurement geometry, and four terminal Hall measurement geometry.	71
2.12	(Left) Actual image of Quantum Design make PPMS (Model-6000 Evercool II) and inside view of sample stage assembly of PPMS Diwar	74
2.13	Actual image of the Quantum Design Incmake MPMS system (Model-MPMS3).	75
3.1	(a) Schematic diagram of the $\text{Sb}_2\text{Te}_3/\text{Ru}/\text{CFB}/\text{Ru}$ heterostructure grown on the sapphire substrate, (b) X-ray diffraction (XRD) spectra of SCR sample measured in Bragg-Brentano mode ($q-2q$ scan), and (c) & (d) show TOF-SIMS depth profiles, from top most layer of Ru to the bottom Al_2O_3 (0001) substrate, encompassing the intermediate layers of CFB, Ru and Sb_2Te_3 . in two representative samples SR2CR and SR8CR, respectively.	85
3.2	(a) Magnetic field dependency of magnetoconductance of bare Sb_2Te_3 , fitted by HLN model. (b) Topological prefactor extracted from HLN equation as a function of temperature. (c-d) Magnetoconductance of sample SCR, SR4CR, and Sb_2Te_3 .	86
3.3	(a) FMR derivative spectra for sample CR detected via lockin for various frequency. (b) Linewidth ΔH as a function of frequency (f) for all the samples (c) Variation of applied magnetic field as a function of frequency f and points are extracted from the FMR spectra fitting and then fitted by Kittle equation.	89

- 3.4 (a) Effect of thickness of the Ru interlayer (t_{Ru}) inserted between Sb_2Te_3 and CFB on α_{eff} of the $\text{SR}(t_{\text{Ru}})\text{CR}$ heterostructure sample. The dashed line corresponds to the case of RCR sample in which both Ru layers are 4 nm thin. (b) M-H hysteresis loops recorded on heterostructures of different types, namely the CR, RCR, SCR, and SR4CR. **91**
- 3.5 Microstrip waveguide measurement setup for measuring the spin pumping induced inverse spin Hall voltage signal V_{mix} on a FM/NM bilayer sample. **92**
- 3.6 (a) Spin pumping voltage signal for sample SR4CR at 5GHz and 5dBm power for +H and -H. (b) Spin pumping signal resonance field comparison with FMR signal at 5 GHz (c) the field dependence of the $(V_{\text{mix}}-V_{\text{offset}})$ -signal measured for sample SCR (black), SR4CR (blue) and SR8CR (orange), normalized by the product of the resistance R and width W of the Sb_2Te_3 layer. (d) Comparison of 2D charge current density J_C^{2D} versus $H-H_r$ responses for all the samples extracted from the symmetric component of V_{mix} signal. (e), (f) Schematic showing the injection of a spin current into the Rashba interface via the thin Ru(2nm) and Sb_2Te_3 . The spin current enters into the Sb_2Te_3 through thin Ru intralayer but diffuse in the thicker Ru intralayer as shown in (f). (g) Dirac dispersion cone of the surface/interface states of Sb_2Te_3 (TI). Injection of a spin current density J_S along z -direction (spin polarized along y -direction) into the TI is shown in right bottom. The TI surface induces an extra population on one of the sides of the Fermi contour (along the x -direction), and therefore a charge current density J_C^{2D} gets induced. **97**
- 3.7 Figure 3.7: (a) Schematic illustration of the experimental configuration employed for the longitudinal spin Seebeck effect measurements performed at room temperature on TI/NM/FM/NM heterostructures, e.g. $\text{Sb}_2\text{Te}_3/\text{Ru}/\text{CoFeB}/\text{Ru}$. (b) Comparison of the field dependences of voltage $V_y (=V_{\text{ANE}}+V_{\text{LSSE}})$ generated corresponding to an out of plane thermal gradient of 10K for the RCR, SC, SCR, SR4CR, SR8CR heterostructures, and uncapped single layer CFB film. The measured voltage data is normalized w.r.t. the width of the samples. (c) Typical $V_y(H)$ loop recorded on the SR4CR sample for different values of out-of-plane temperature gradients ($\Delta T= 5\text{K}, 10\text{K}, 15\text{K}$ and 20K). Inset shows the **103**

temperature-gradient dependence of the saturated Seebeck voltage corresponding to 100 Oe field as recorded on SR4CR sample. (d) Comparison of dependence of the maximum power generated as a result of SCC (PSCC) due to LSSE and ANE effects on the out-of-plane temperature gradient maintained on for bare CFB film, RCR and NCN heterostructures (with and without TI Sb_2Te_3 and Bi_2Te_3). Inset shows the bar-graph comparison plot of the maximum power for all the different samples at ($\Delta T= 10\text{K}$). (e) Schematic of the equivalent model of the SR4CR heterostructure subjected to a temperature gradient (top to bottom) acting like an overall voltage source V_y , resulting from the various parallelly connected resistances with the respective series voltage-sources due to ANE and LSSE effects with specific polarities as shown. (f) Schematic visualization of the spin accumulation in a typical TI/NM/FM/NM such as $\text{SR}(tr_u)\text{CR}$ heterostructure when subjected simultaneously to a temperature gradient and a transversely applied magnetic field high enough to saturate the FM layer.

- 4.1** Growth and characterization of heterostructure bilayer stacks shown in table 4.1: (a) Schematic showing the sequence of steps undertaken in growing the heterostructure by sputtering with Au contacts pads required for electrical measurements. (b, c) Depth profile spectra (TOF-SIMS normalized intensity vs sputter time) of $\text{Zr}(4.5)/\text{CFB}(20)$ and $\text{Zr}(4.5)/\text{Pt}(2)/\text{CFB}(20)/\text{Pt}(2)$ heterostructures. **119**
- 4.2** Schematic Representations of Spin and Orbital Current Generation and their Charge Conversion in Zr/CFB Heterostructures: (a) Schematic illustration of the spin and orbital pumping phenomenon in the Zr/CFB heterostructure. Spin current is generated in the ferromagnetic CFB layer, where the spin current in the bulk of CFB intertwines with the orbital angular momentum due to the moderate SOC strength of CFB. This process generates both spin and charge current simultaneously. These currents are pumped into the adjacent Zr layer, where the orbital current is converted into charge current via both the interfacial inverse orbital Rashba-Edelstein effect (IOREE) at the Zr/CFB interface and the inverse orbital Hall effect and inverse spin Hall effect within the bulk of Zr. **(b)** **121**

Schematic depiction of spin and orbital currents in the Zr/CFB/Zr structure. Spin and orbital currents are injected in both upward and downward directions into the Zr thin layers. Due to the ISHE, the spin current in the top Zr layer flows in the opposite direction compared to the bottom Zr layer. Similarly, driven by the IOHE, the orbital current in the bulk Zr flows in opposite directions for the top and bottom Zr layers. At the two Zr/CFB and CFB/Zr interfaces of CFB layer, the orbital currents get converted into charge current in the same direction via the IOREE effect. **(c)** Schematic of spin-to-orbital conversion in Zr/Pt/CFB, where a Pt layer is inserted between the Zr and CFB layers. Here, the spin and orbital current generated by the spin-orbit pumping phenomena in CFB layer transferred into the adjacent Pt layer. The spin current directly converted into charge current due to inverse spin Hall effect in high SOC Pt layer, whereas remaining pure orbital current transfer into the adjacent Zr layer and convert into the charge current via IOREE and IOHE. **(d)** Schematic showing the cancellation of ISHE-induced voltage by the opposing polarity in a symmetric Pt/CFB/Pt structure. In this stack, the ISHE-generated spin currents from the top and bottom Pt layers cancel out each other, resulting in a net current that is purely orbital in nature, which eventually contribute to the charge current in Zr via IOREE and IOHE.

4.3 Spin-Orbital Pumping and Charge Conversion Analysis in Zr/CFB and Zr/Pt/CFB stacks: **124** (a) Measured charge current in the Zr(4.5)/CFB(20) sample, generated through spin-orbital pumping, using a microstrip-based waveguide at an RF power of 5 dBm. (b) Measured charge current in the Zr(4.5)/Pt(2)/CFB(20)/Pt(2) sample, where opposing ISHE and IOHE contributions from the top and bottom Pt layers are cancelled, isolating the charge current produced via the IOREE in the Zr layer. (c) Measured charge current in the Zr(4.5)/Pt(2)/CFB(20) sample, where the insertion of a Pt layer enhances the total charge current by generating pure orbital current through the high spin-orbit coupling of Pt. This orbital current is converted into charge current in the Zr layer via the IOREE effect. (d) Generation of charge current as a function of magnetic field, in which the charge current is higher at the resonance field of the sample

Zr(2)/CFB(20). This generated current is fitted by the symmetric and antisymmetric of the Lorentzian function of given equation (3.9). (e) Bar graph displaying the charge current contributions from spin and orbital currents across different samples. The charge current remains nearly constant for the Zr thickness of the Zr(t)CFB(20) samples, indicating interface-dominated conversion, while a notable increase is observed when a Pt layer is inserted between Zr and CFB, due to the enhanced orbital contribution.

4.4 (a) & (b) Dependence of spin orbital current density J_{LS} and effective orbital Edelstein length λ_{IORE}^{Zr-eff} with the thickness of Zr layer t_{Zr} in Zr(t)/CFB(20) and Zr(t)/Pt(2)/CFB(20)/Pt(2) heterostructure series. (c) Dependence of effective Gilbert damping constant as a function of FM CFB layer thickness t_{CFB} in the CFB(t), Zr(4.5)/CFB(t), Pt(2)/CFB(t)/Pt(2), and Zr(4.5)/Pt(2)/CFB(t)/Pt(2) sample series. (d) Effect of t_{CFB} on the spin orbital current J_{LS} in the Zr(4.5)/CFB(t) and Zr(4.5)/Pt(2)/CFB(t)/Pt(2) samples series. (e) Effect of t_{Zr} on the λ_{IORE}^{Zr-eff} in the Zr(4.5)/CFB(t) and Zr(4.5)/Pt(2)/CFB(t)/Pt(2) sample series. (f) Effect of thickness of Pt insertion layer (2nm & 10 nm) on the generated charge current I_C in the Zr(4.5)/Pt(2)/CFB(20)/Pt(2) and Zr(4.5)/Pt(10)/CFB(20)/Pt(10) samples. The I_C is found to get suppressed in presence of thicker insertion layer of Pt. While the symbols represent the calculated data of various parameters, the solid lines are guide to the eye for the observed trend in the data.

4.5 Longitudinal Spin-Orbital Seebeck Effect (LSOSE) and Charge Current response and their comparative analysis in Zr/CFB and Zr/Pt/CFB heterostructures: (a) Schematic illustration of the measurement setup for the spin Seebeck effect, where an out-of-plane temperature gradient (ΔT) is applied across the Zr/CFB heterostructures. Total charge current ($I_{LSOSE+ANE}$) as a function of the applied magnetic field for the samples is shown in (b) Zr(4.5)/CFB(20), (c) Zr(4.5)/Pt(2)/CFB(20), and (d) Zr(4.5)/Pt(2)/CFB(20)/Pt(2), measured at various temperature gradients ($\Delta T = 5, 10, 17, 26$ K). The voltage/current was measured in the saturation regime of CFB. (e) Comparison of total charge current ($I_{LSOSE+ANE}$) as a

- function of temperature gradient across different samples at saturation magnetization conditions, indicating the contributions from both spin and orbital effects. (f) Comparison of total generated current ($I_{LSE+ANE}$) at $\Delta T = 10$ K, for all the measured samples, showcasing the enhancement of the orbital current contribution due to the presence of Pt.
- 4.6** Comparison of effective Rashba Edelstein length λ_{IRE}^{eff} , determined using spin pumping FMR measurements, in different heterostructures as reported in literature with the present work. The λ_{IORE}^{Zr-eff} values for Zr/CFB and Zr/Pt systems are comparable to those reported in TIs and HMs. This is due to the joint contributions from the spin pumping as well as the orbital pumping mechanisms in the former. **135**
- 5.1** (a) Schematic of the co-sputtering process employed for deposition of the CrTe₂ thin film. (b) EPMA elemental mapping image of Cr and Te using recorded (at 15keV energy) over 90×120 μm² area. (c) The XRD patterns (recorded in $q-2q$ mode) of the LC-CT-60 and HC-CT-60 films, both exhibiting the diffraction peaks only from the $(0\ 0\ l)$ family of planes (Peaks from Si($l\ 0\ 0$) substrates are marked as \ddot{A}). The intensity of the diffraction peaks is visibly more intense for HC-CT films. (d) The Raman spectra (recorded at room temperature) of the LC-CT and HC-CT samples. **147**
- 5.2** (a) Temperature dependence of the magnetization response of a representative LC-CT-60 film recorded for both the zero-field cooling and field cooling protocols in presence of 2 kOe magnetic field applied in out-of-plane and in-plane directions. (b-d) Temperature dependent OOP magnetization hysteresis loop of samples of the LC-CT series. The presence of a kink-like feature observed in case of LC-CT-20 sample at 2K is due to the centring issue in this particular sample. (e) Comparison of the IP and OOP magnetization hysteresis loops of the LC-CT-60 sample recorded at 2K, clearly showing that the easy axis of the magnetization is oriented in the out-of-plane direction. **149**
- 5.3** (a) Out-of-plane and in-plane field-cooled magnetic-moment of the HC-CT films as a function of temperature observed in presence of 10kOe field. (b-d) Temperature dependent hysteresis loops of the samples HC-CT series films measured in the OOP direction. (e) Hysteresis curves recorded **151**

	in IP field configuration at various temperatures in 2-200K range for the HC-CT-60 sample for comparison with the OOP hysteresis loop data in 3(d). (f) Temperature dependent OOP coercivity of HC-CT and LC-CT samples extracted from their respective m-H loops. Similar plots deduced from AHE data are presented in Figs. 5.4 & 5.5). (g-i) Comparison of the normalised hysteresis loops recorded in OOP field configuration at 2K for HC-CT-20, HC-CT-40, and HC-CT-60 samples (see text for more details).	
5.4	The temperature dependence of the OOP magnetoresistance loops (a-c) and Hall-resistivity ρ_{xy} -H loops (d-f) of the LC-CT-40 and LC-CT-60 samples.	153
5.5	The temperature dependence of the OOP magnetoresistance loops (a-c) and Hall-resistivity ρ_{xy} -H loops (d-f) of the HC-CT-20, HC-CT-40, and HC-CT-60 films.	154
5.6	(a) Temperature dependent longitudinal resistivity of the samples of HC-CT and LC-CT series. (b), (c), (d), (e) and (f) shows the temperature dependence of the Remanent anomalous Hall resistivity (ρ_{xy}^0), Ordinary Hall coefficient (R_0), anomalous Hall coefficient (R_S), anomalous Hall conductivity (σ_{AH}), and the anomalous Hall angle (θ_{AH}) of the LC-CT-60 and HC-CT-60.	157
6.1	(a) Schematic of film deposition via magnetron sputtering (b) x-ray diffraction patterns, recorded in coupled θ - 2θ mode, for the samples HC-CT60/BT15 and LC-CT60/BT15 show the identical peak positions for both the samples (c) TOF-SIMS depth profile of LC-CT60/BT6 sample (d) Schematic illustration of CrTe ₂ /Bi ₂ Te ₃ heterostructure formation by Cr and Te atom and Bi and Te atoms into a van der Waals structure.	168
6.2	(a, b, & c) Magnetic field dependence of anomalous Hall resistivity of the LC-CT60/BT6, LC-CT60/BT10, and LC-CT60/BT15 heterostructure at different temperature under the out of plane magnetic field. (d) The anomalous Hall resistivity behaviour with the out of plane magnetic field in which a 2 nm thick Te layer was inserted to break the SOC effect between CT and BT layer.	171

6.3	(a) The measured transverse Hall resistivity data for LC-CT60/BT6 (T=2K). (b) The extracted contribution to the overall $\rho_{xy}(T)$ from the pure topological Hall resistivity at 2K for LC-CT60/BT6. (c & d) Color contour plot of the extracted topological Hall resistivity as a function of temperature for LC-CT60/BT6 and LC-CT60/BT10. HC(T) from M(H, T) is also displayed to show a perfect overlap.	173
6.4	(a-c) magnetic field dependence of anomalous Hall resistivity at various temperature for the samples HC-CT20/BT15, HC-CT40/BT15, and HC-CT60/BT15, respectively. The blue and red data symbols represent the decreasing and increasing magnetic field recording cycles.	175
6.5	(a) Schematic illustration of magneto-transport measurements for AHE and MR (b) Temperature dependent out of plane magnetoresistance for the LC-CT/BT and HC-CT/BT heterostructures as a function of magnetic field.	176
A1.1	(a) The XRR spectra of Zr(t)/CFB (20nm) bilayers with $t_{Zr} = 2, 3, 4.5, 6, 10 \text{ nm}$. The symbols represent the experimental data, while the lines represent the simulated spectra. (b) TOF-SIMS depth profile spectra of sample Zr(4.5)/Pt(2)/CFB(20). (c) Frequency-dependent FMR spectra recorded on the Zr(4.5)/CFB(20) samples. (d) Variation of linewidth with the resonance frequency for the samples Zr(t=2, 3, 4.5, 6, 10 nm)/CFB(20) Zr(4.5)/Pt(2)/CFB(20)/Pt(2), and Zr(4.5)/Pt(2)/CFB(20) fitted by the linear equation. (e) Frequency-dependent variation of resonance field H_r for samples Zr(t=2, 3, 4.5, 6, 10 nm)/CFB(20). (f) Variation of effective damping constant and effective magnetization with the increase of Zr film thickness t_{Zr} .	186
A1.2	(a-c) Line width as a function of frequency of the CFB thickness dependent series CFB(t), Pt(2)/CFB(t)/Pt(2) and Zr(4.5)/Pt(2)/CFB(t)/Pt(2) respectively to find the effective Gilbert constant. (d) Thickness dependent MH curve of the CFB(t) to calculate the saturation magnetization M_S	188
A2.1	(a-e) Measured raw data signal for the thickness-dependent series for Zr(t=3, 6, 10, 15, 20 nm)/CFB(20) the voltage was measured and current was plotted by dividing the resistance of sample (f) Pumping signal for CZ4.5C and Z4.5CZ4.5 sample, in which spin-orbital current is injected	190

- from the both top and bottom direction into the Zr. (g) Spin to charge current I_C signal as a function of applied magnetic field for the sample Pt(2)/CFB(20), CFB(20)/Pt(2), and Pt(2)/CFB(20)/Pt(2) (h) Measured pumping signal for CFB/CuOx heterostructure to verify the generation of orbital current from the CFB layer. (i) Measured charge current signal for the pure CFB(20) thin file to investigate the self induced ISHE signal in the CFB layer.
- A2.2** (a-e) Spin orbital to charge current conversion in the ferromagnetic CFB thickness variation series Zr(4.5)/CFB(t=3, 5, 7, 10, 15) at a constant Zr thickness of 4.5 nm. **191**
- A2.3** (a-d) Orbital to charge conversion of the sample series Zr(4.5)/Pt(2)/CFB(t)/Pt(2), in which CFB thickness is varying and generate pure orbital current through Pt layer into the Zr. (e) Orbital to charge current behaviour for a constant thickness of CFB(20) and varying the Zr thickness in the sample series Zr(t=2, 6, 10, 20)/Pt(2)/CFB(20)/Pt(2) (f) Orbital to charge current comparison in the sample Zr(4.5)/Pt(2)/CFB(20)/Pt(2) and Zr(4.5)/Pt(10)/CFB(20)/Pt(10), where the thickness of platinum is much higher than the spin diffusion length. (g-h) $1/t$ CFB dependent of the charge conversion efficiency and the effective Gilbert damping constant. **192**
- A3.1** (a-d) LSOSE Curves for thickness-dependent of Zr layer in which thickness is varied from 2-10nm in the samples Zr/CFB names as Zr(2)/CFB(20), Zr(3)/CFB(20), Zr(6)/CFB(20), and Zr(10)/CFB(20), respectively. The LSOSE signal is measured for different temperature gradients at ($\Delta T=5, 10, 17, 26K$) for all the samples. (e) The LSOSE signal for the sample CFB(20)/Zr(4.5)/CFB(20), in which a thermally generated spin orbital current is sent from the top and bottom directions into the Zr. (f) ANE current signal generated from the pure FM layer of CFB at different temperature gradients. **194**
- B1.1** Photographs showing the severe flooding incident that damaged the PPMS laboratory facility. The images illustrate water ingress into the experimental room, leading to partial submersion and displacement of the PPMS equipment, cryostat chamber, and associated electronic systems. **197**

The event caused significant disruption to ongoing experimental work and necessitated a prolonged shutdown and restoration process.

- B1.2** Restoration and reassembly process of the PPMS sample probe and cryostat components. (a) PPMS Diwar assembled with the coldhead and superconducting magnet with probe assembly (b) Superconducting magnet with their electrical connection feedthrough and VTI (c) Diwar after removing the coldhead and magnet from it and removing the water from inside the diwar after submerged. (d) 4K coldhead cleaning and servicing to remove the water and humidity and cleaning of the cernoc sensor. These steps were essential for ensuring safe operation and recovery of the system for subsequent experimental measurements. **198**
- B1.3** Reconditioning of the PPMS sample probe assembly after flood-induced damage. (a) Sample probe assembly with electrical feedthrough connections for transport and magnetic measurements. (b) Resistive wire heater integrated around the probe for precise temperature control during measurements. (c) Repair of the Cernox temperature sensor located near the sample position, with newly soldered electrical leads. (d) Residual water droplets observed inside the cold-head chamber of the dewar, indicating moisture accumulation following submersion. **199**
- B1.4** Inspection and repair of the HLC4500 helium closed-cycle compressor system following water-induced damage. (a) Three-phase He closed-cycle compressor unit. (b) Internal electronics of the compressor assembly, including the three-phase variable-frequency drive (VFD) for compressor power control and the single-phase VFD used for operating the cold-head motor. (c) Compressor controller card responsible for remote communication and system monitoring, enabling software-based readout of parameters such as supply and return He pressure, cooling-water temperature, and operational hours. (d) Single-phase VFD electronics damaged due to flooding, which could not be repaired locally. (e) Faulty resistor identified on the controller card and replaced locally to restore system functionality. **200**
- B1.5** Pump control system repair and restoration process following flooding damage. (a) ECII controller unit responsible for regulating the pumping **202**

system and electromagnetic valve operation. (b) Internal electronics of the ECII controller, which were cleaned and successfully repaired after water intrusion. (c) Electromagnetic valve assembly following restoration. (d) Scroll pump after drainage and moisture removal. (e-f) Disassembly of the scroll pump revealing water accumulation inside the pumping chamber, followed by cleaning and reassembly. (g-h) Pump motor of the water chiller showing corrosion and mechanical wear, undergoing servicing and repair.

- B1.6** Recommissioning and performance validation of the PPMS system after complete servicing. (a) Restored PPMS laboratory setup following full disassembly, cleaning, and reinstallation of damaged components, successfully brought back into operational condition. (b) AC transport measurement: resistivity versus temperature curve (2-300K) of a thin film recorded after system recovery, demonstrating reliable temperature-dependent behavior. (c) Temperature-dependent (2-300K) anomalous Hall effect (AHE) loops confirming magnetic characteristics in the field range (5T). (d) Room-temperature magnetization (M-H) hysteresis curve of the thin film measured in VSM after-repair, indicating proper functioning of the superconducting magnet and sample-probe assembly. **203**
- B2.1** (a) High vacuum sputtering system associated with the RHEED insitu characterization. (b) Burn filament of RHEED (c) Electric tungsten bulb (d) Filament made by using bulb (e) Filament holder cage **206**
- B2.2** (a) Electron source (b) First spot of electron beam seen after new home built filament (c) Electron diffraction pattern of Si with new filament (d) Old CRT tube (e) Cutting of CRT screen for fitting in the RHEED frame (f) Screen after fitting into the frame (g) Diffraction pattern with new screen. **207**

List of Tables

Table No.	Table Caption	Page No.
1.1	List of some important heterostructures comprising of either NMs, HMs or TIs and Ferro/Ferrimagnets together with the values of their effective spin mixing conductance (g_{eff}) and spin to charge conversion efficiency parameter (λ_{IEE}) and growth method employed in synthesising them.	36
1.2	List of orbital Hall efficiency of the pure elements and their heterostructures.	37
1.3	List of van der Waal materials with their T_c and magnetic ordering.	38
3.1	Growth parameters for fabricating the heterostructure.	83
3.2	Details of samples of different series together with their name code. The letters S, B, C, R, and N used in the sample code refer to Sb_2Te_3 , Bi_2Te_3 , CFB, Ru and Nb, respectively. While individual layer thicknesses (in nm) of S, B, C and N are respectively fixed at 20, 20, 20 and 10 nm (as specified in parenthesis), the Ru interlayer thickness (t) is varied from 0 to 12 nm. A passivating layer of Ru (Thickness 4nm) is sputtered on top of almost all the samples of the different heterostructure-series.	84
3.3	Values of various parameters determined from the FMR and ISHE measurements performed on different heterostructure samples: the effective damping constant α_{eff} , spin pumping voltage (V_{SP}), width (W), resistance (R), effective spin mixing conductance ($g_{eff}^{\uparrow\downarrow}$) of the Sb_2Te_3 layer and the charge current density J_C^{2D} from the SCC effect.	94
3.4	A summary of previously reported values of g_{eff} and spin to charge efficiency λ_{IEE} measured by FMR and SPFMR in stacks with trivial and non-trivial topological materials together with those found in the present case of $Sb_2Te_3/Ru/CoFeB/Ru$. The data reported in the present work are comparable with the literature values.	98
3.5	A summary of previously reported efficiency of spin Seebeck generated power. The power generated via spin Seebeck measurements was	105

compared with the topologically non-trivial materials and our observation of the generated power is much higher than the previously reported value. Here we are comparing the efficiency of the device in terms of power, while in the literature, they show the enhancement in terms of generated voltage. The generated voltage can be enhanced by the higher internal resistance of the device. So, in the given table we compared with the generated power by converting formula of $P = V_{LSS}^2/R$. The data reported in the present work are comparable and higher with the literature values.

4.1	The details several heterostructures series fabricated on the sapphire Al_2O_3 (0001) substrate at room temperature growth are shown in the table below.	117
5.1	Details of the CrTe_2 film samples of the LC-CT and HC-CT series (Film thicknesses and growth temperatures T_S).	146
5.2	Comparison of the Curie temperature of sputter-grown 2D ferromagnetic films with those prepared using other growth techniques	158
6.1	Details of the $\text{CrTe}_2/\text{Bi}_2\text{Te}_3$ film samples of the L-CT/BT and H-CT/BT series (Film thicknesses variation of BT).	169
A2.1	Values of various parameters determined from the FMR and ISHE measurements performed on different heterostructure samples: the effective damping constant α_{eff} , spin orbital current density (J_{LS}), generated total charge current density (J_c^{2D}), effective spin mixing conductance ($g_{effS}^{\uparrow\downarrow}$), and the effective inverse Edelstein length λ_{IORE}^{eff} which have both IOREE effect and Orbital Hall angle in terms of Edelstein length and ISHE efficiency converted into the IEE length contribution calculated by ration of total pumped spin current (J_{LS}) and total charge current (J_c^{2D}) of the Zr, and Pt/Zr layer of the given stack below.	193